Modeling Capillary Condensation Hysteresis Cycles in Reconstructed Porous Media

František Štěpánek and Miloš Marek
Dept. of Chemical Engineering, Prague Institute of Chemical Technology, Technická 5, 166 28 Praha 6, Czech Republic

Pierre M. Adler
Institut de Physique du Globe de Paris, 4 place Jussieu, 75 252 Paris CEDEX 05, France

A computational algorithm for tracking liquid–vapor interfaces moving with curvature-dependent velocity, based on the Gibbs energy formulation and the level-set approach, is described. The algorithm is used for finding equilibrium distributions of condensate in several samples of 3-D reconstructed porous media under varying relative saturation of the surrounding atmosphere. Primary and higher-order hysteresis cycles are calculated and their dependence on various physico-chemical parameters (temperature, wetting angle) as well as on geometrical properties of the porous medium is investigated. An explanation of the influence of the morphology of a porous medium on the character of corresponding hysteresis loops is provided.

Introduction

Adsorption/desorption hysteresis has been observed in a number of adsorbent–adsorbate systems, and its importance for the characterization of porous solids (such as Bordère et al., 1998; Ravikovitch et al., 1998; Liu et al., 1994), adsorption-based separations (such as Okazaki, 1993), and heterogeneous catalysis (Mann, 1998), has been pointed out. The observed hysteresis effects can be explained by the existence of phase transitions, either the creation of clusters in the surfaceadsorbed phase (the case of molecules with strong lateral interactions), or the ''classic'' vapor–liquid phase transition, that is, capillary condensation in meso- and microporous space of adsorbent or catalyst particles (Jaroniec, 1997). Studies of adsorption hysteresis have been worked out both at the molecular level—Monte Carlo simulations and detailed models of processes taking place inside a single pore (such as Seri-Levy and Avnir, 1993; López-Ramón et al., 1997; Gelb and Gubbins, 1998)—and at the level of ''collective phenomena'' such as percolation (Kainourgiakis et al., 1998). However, systematic studies on the mesoscale, which would allow for direct and flexible calculation of the shape of hysteresis isotherms in the presence of capillary condensation from known physicochemical properties of the adsorbate and geometrical properties of the adsorbent, are still missing.

Figure 1 illustrates the position of mesoscale modeling in the hierarchy of scales as applied to adsorption processes. At the molecular level (not shown in Figure 1), discrete models based on statistical mechanics (such as Müller et al., 1996) can provide physicochemical properties calculated from first principles. These serve as an input for mesoscale models (the subject of this work), which in turn provide data (hysteresis-dependent isotherms, effective diffusion coefficients) for continuum, ''effective-medium'' models at the particle level. Simulations at the process scale then make use of particle models either directly or via volume-averaged approximations, for example, the linear driving force frequently used in the modeling of PSA processes. While active research has been underway for years, both at the molecular level (see the review by Deem, 1998) and at the particle scale (such as Keil, 1996), methodologies for integrating models of different length and time scales have appeared only relatively recently (such as Vlachos, 1997; Sonwane and Bhatia, 1998).

It has become commonplace to approximate the geometry of porous media (and especially adsorbents) by a network of cylindrical pores, characterized by certain pore-size distribution and mean connectivity. These models, however, do not provide an accurate representation of real porous structures. An alternative approach to the description of the geometry of porous media is based on the concept of phase functions, spatially correlated random fields, and their reconstruction

Correspondence concerning this article should be addressed to M. Marek.

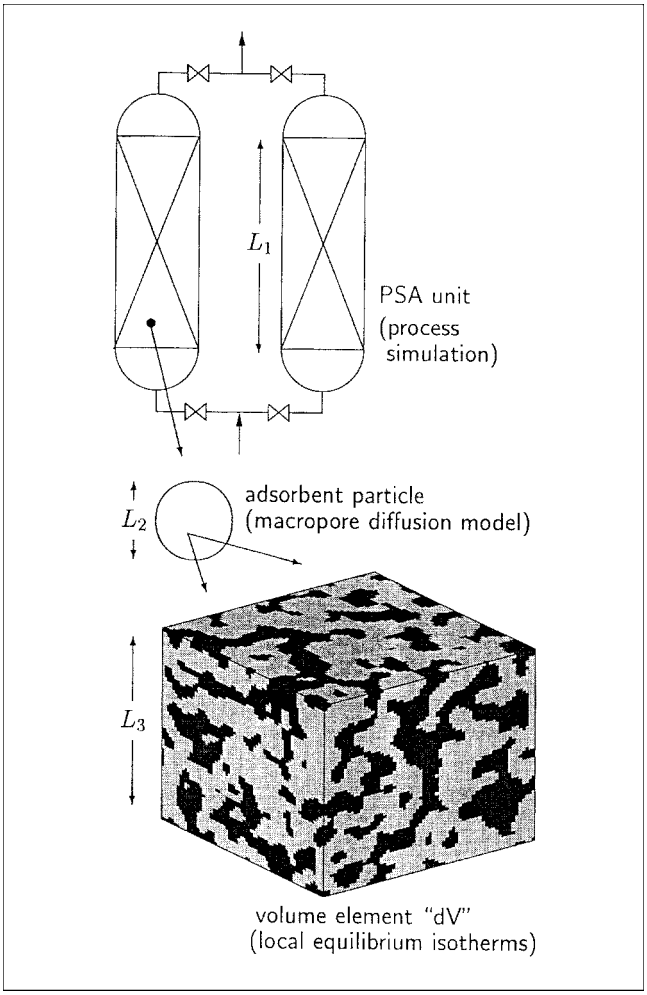

Figure 1. Hierarchy of scales in the modeling of adsorption processes ($L_1 \gg L_2 \gg L_3$).

(Adler, 1994; Adler and Thovert, 1998), cf. also the ''quench'' method of Gelb and Gubbins (1998). This approach gains in importance, especially as sophisticated image-analysis techniques and equipment become widely available (such as Zhou et al., 1998) together with the increasing power of computer hardware and software.

The purpose of this work is to demonstrate a computational algorithm for the determination of equilibrium distribution of condensate in a reconstructed porous medium under varying partial pressures of the condensable component in the surrounding atmosphere. Such an algorithm can serve as a tool for direct estimation of the shape of hysteresis-dependent adsorption isotherms from known morphology of a porous medium under varying external conditions, namely, temperature (cf. Ball and Evans, 1989). This information is needed as an input for the calculation of optimum operating parameters of industrial processes employing porous media, such as air drying by pressure-swing adsorption (Štěpánek et al., 1999). Obtaining the data by experiments in the whole range of operating conditions (temperatures, pressures, different adsorptives) can be rather expensive. Thus it is advantageous to characterize the geometric properties of a given porous medium (adsorbent or catalyst particle) only once (such as via image analysis), and then perform computer simulations in a reconstructed porous medium for the desired external conditions. Of course, this methodology is not aimed at replacing experiments entirely; its purpose is to provide relatively accurate and inexpensive estimates of adsorption hysteresis behavior for a wider range of physicochemical parameters.

The problem addressed by this work belongs to a larger class of problems—those involving sufficiently realistic, yet ''operational'' from the engineering point of view, description of systems in which there is a coupling between the geometrical properties of a porous medium and the physicochemical processes (reaction, sorption, phase transition, diffusion, convection, etc.) taking place in it. Apart from adsorption-based separations accompanied by capillary condensation, other examples are processes within porous catalysts (such as the growth of polymer particles in fluidized-bed reactors for polyolefin production), catalyst deactivation by coking (as in FCC), or three-phase reactors (such as those used for hydrogenations). Cases where the dissolution of a porous medium is accompanied by convective transport have been addressed by, for example, Békri et al. (1995) or Fredd and Fogler (1998);Ostrovskii et al. (1994) considered the influence of capillary condensation on heterogeneously catalyzed reactions.

Problem Formulation

Let us consider a closed system consisting of a sample of a porous solid material surrounded by a gaseous atmosphere containing two components, one above its critical point and one in the form of a condensable vapor. Let the volume of the solid sample be much smaller than that of the whole system, so that any vapor–liquid phase transitions occurring in the pore space of the sample have a negligible effect on the composition of the surrounding atmosphere, as well as on the total temperature and pressure (an approximation of such a system could be a gravimetric chamber of the McBain type). Finally, let the characteristic dimensions of the pore space inside the solid sample be such that interface curvature effects are significant in determining the equilibrium vapor pressure, in the order of nanometers to tens of nanometers, depending on the nature of the condensate. Any external force fields, such as gravity, are considered to be absent or their effects negligibly small compared to those of the other forces present, namely interfacial tension. As a result of interfacial tension, the system tends to minimize its free surface A for a given volume of condensate V. A sphere is well known to be the geometrical object with minimum surface-to-volume ratio, for which holds $dA/dV = 2/r$. Given that the volumetric work is pdV and the surface expansion work γdA, a pressure difference $\Delta p = 2\gamma/r$ (the well-known Young-Laplace equation) is required to maintain a stable spherical interface of radius r; γ is the liquid–gas interfacial tension (hereafter called simply surface tension).

The condition for thermodynamic equilibrium in a closed system under constant temperature and pressure requires that the total differential of the Gibbs energy be equal to zero

$$dG = \mu_l dn_l + \mu_g dn_g + \gamma dA = 0 \qquad [T, P], \qquad (1)$$

where μ_i are the partial molar Gibbs energies $(\partial G/\partial n_i)_{T,P,n_{j\neq i}}$, that is, the chemical potentials; the subscripts l and g denote liquid and gas, respectively. The integral relations for the chemical potentials are

$$\mu_g = \mu_g^0 + RT \ln(p) \tag{2a}$$

$$\mu_l = \mu_g^0 + RT \ln(p_s), \tag{2b}$$

where fugacities were replaced by partial such as pressures; μ_g^o is the chemical potential at a reference state (such as STP), and p_s is the saturated vapor pressure at temperature T (above a flat interface). Since $dA = (2/r)V_m dn_l$ (V_m being the molar volume of the liquid), and $dn_l = -dn_g$ at equilibrium, one obtains the following relationship between the interface curvature radius and the equilibrium vapor pressure above it, p^*

$$p^* = p_s \exp\left[-\frac{2\gamma}{r}\frac{V_m}{RT}\right]. \tag{3}$$

This relationship is known in the literature as the Kelvin equation. For convex interfaces, $p^* < p_s$, while for concave ones, $p^* > p_s$; the curvature radius r is conventionally taken as negative for concave interfaces. Thus, concave interfaces tend to evaporate spontaneously, while either condensation or evaporation can occur on a convex interface, depending on its curvature and the total pressure and composition of the vapor phase.

While for freely dispersed droplets or cavities, the solution of the ''phase distribution'' problem is relatively simple, since it is given by Eq. 3, the situation gets more complicated when interactions with a solid phase and its wettability are to be taken into account. Although analytical solutions can be found in some regular geometries (such as Dobbs et al., 1992), a numerical solution is required in a general three-dimensional (3-D) porous medium. The objective of this work was to develop and implement an algorithm that converges to an equilibrium distribution of liquid and vapor phases within a 3-D porous medium, given the geometry of the medium and the following physicochemical parameters: the temperature T, total pressure P, and the mole fraction y of the condensable vapor in the atmosphere surrounding the sample, the liquid–solid wetting angle ϑ, the saturated vapor pressure $p_s(T)$, given, for example, by the Antoine equation, the surface tension $\gamma(T)$ of the liquid, and its molar volume $V_m(T)$. The equilibrium phase distribution is defined as a partition of the vapor and the condensate in the pore space of the solid sample, such that (1) the curvature of all menisci (gas–liquid interfaces) adjacent to a vapor phase that belongs to the same percolation cluster as the sample surroundings, satisfies Eq. 3 with $p^* = yP$, and (2) the contact angle ϑ holds at all gas–liquid–solid intersections.

Implementation

Let us introduce a phase function $X : \mathbf{S} \rightarrow \mathbf{A}_n$, encoding the phase distribution by assigning a symbol $a \in \mathbf{A}_n$ (where $\mathbf{A}_n$ is an n-membered finite alphabet, and n is the number of phases) to every point $x \in \mathbf{S}$ (where $\mathbf{S} \subset \mathbf{R}^3$ is a part of the Euclidean space representing our system of interest, cf. Figure 1). The algorithm is based on locally simulating the process of interface growth (cf. the simulated annealing approach of Silverstein and Fort, 1998), and proceeds in the following way. The set $\mathbf{S}$ is discretized into a set of finite volumes (cubic volume elements were chosen in this work); the phase-encoding alphabet is $\mathbf{A} = \{s, l, f, g\}$ (meaning solid, liquid, interface, and gas, respectively). In addition, a value $s_i \in (0; 1)$ expressing the volume fraction of condensate in the ith discretization element (its ''saturation'') is assigned to every interface point. Moreover, points belonging to the interface and vapor phase also keep information about the composition of the gas phase (the mole fraction y of the condensable component) and the identity of the percolation cluster to which they belong (as a result of interface growth, closed cavities not connected to the bulk phase can emerge). Concentration gradients in the gas phase are not considered, the values of y in the pore space connected to the surface are not ''depleted'' by condensation, since the surrounding atmosphere serves as an infinite reservoir. The overall material balance of the condensable component is satisfied in closed cavities.

Interface displacements are curvature-dependent; the curvature radius r is calculated by locally approximating the interface by an elliptic paraboloid oriented so that its axis is identified with the liquid–gas interface normal vector. A radius corresponding to the mean curvature in two orthogonal directions is used for equilibrium vapor pressure calculations from the Kelvin equation. The relationship between the second spatial derivative of s and the corresponding radius r in the ith finite volume in one direction is

$$\frac{1}{r_i} = \left.\frac{\partial^2 s}{\partial z^2}\right|_i \approx \frac{s_{i-1} - 2s_i + s_{i+1}}{h^2}, \tag{4}$$

where h is the side of the elementary cube, and the second-order symmetric difference formulas are used for calculating the second derivatives. Concave interfaces ($\partial^2 s/\partial z^2 < 0$) lead to negative radii, and convex interfaces give positive values of r (cf. discussion following Eq. 3). Before calculating the curvature, though, the interface orientation has to be determined by searching the nearest neighbors of the current discretization element and orienting the normal vector so that it points from liquid to gas; special care has to be taken in ''singular'' situations such as sharp corners of solid, interfaces approaching each other from opposite directions, or tips of liquid. In every iteration, the equilibrium vapor pressure p_i^* corresponding to the local curvature radius is calculated according to Eq. 3, and the interface is displaced by δs_i

$$\delta s_i = k\frac{1}{h}\frac{V_m}{RT}(p - p_i^*)\delta t, \tag{5}$$

where k is a rate parameter and δt a virtual time step. Although formally equivalent to a relationship that would describe the kinetics of liquid–vapor phase transition in the absence of diffusional limitations, Eq. 5 should be treated as a numerical scheme only. The parameters k and δt are chosen according to the required precision and the speed of convergence, while numerical stability has to be kept in mind, since too high values of these parameters can lead to noncon-

vergence. The interface evolution from iteration to iteration does not correspond to real time. If s_i updated according to Eq. 5 in a given finite volume element exceeds unity, all nearest-neighbor vapor-phase points get labeled as interface ones (again various "singular" situations must be accounted for, especially the possible emergence of a new closed cavity); if s_i drops below zero, the current point becomes vapor-phase (unless it is adjacent to solid, in which case it remains an interface point even if it "dries out" completely), and its liquid nearest neighbors become interface points.

Interface positions at the gas–liquid–solid interface are updated according to the same formula as "ordinary" interface points; the contact angle comes into play during the calculation of the curvature radius. After the interface orientation is determined, an s value is also assigned to the relevant subset of points belonging to the solid phase, in such a way that the wetting angle ϑ be locally satisfied. The relationship between ϑ and the gradient of s at the fluid–solid interface is

$$\cot\vartheta = \left.\frac{\partial s}{\partial z}\right|_{i+1/2} \approx \frac{s_{i+2} - s_{i+1}}{h}. \qquad (6)$$

Once s_{i+1} is expressed using this equation, the curvature radius r can be calculated according to Eq. 4 and the interface position updated using the same scheme (Eq. 5) as for "ordinary" points, not adjacent to the solid wall. This approach automatically ensures that for small ϑ (that is, highly wettable solids), the gradient of s at the solid wall will be high, which will also increase the absolute value of the curvature. The radius r, inversely proportional to the curvature (cf. Eq. 4) will thus be small, leading to small p^*, that is, high driving force for condensation ($p - p^*$). The meniscus will then be dragged along the solid interface until it reaches a point where the solid-surface curvature is such that the wetting angle is satisfied, that is, the curvature radius calculated using a solid-phase s value determined according to Eq. 6 leads to p^*, which is in equilibrium with p. For hydrophobic solids, the situation is analogous, except that the liquid interface is "pushed down" rather than "pulled up" along the solid. Apart from being an efficient computational procedure, assigning a value s to points belonging to the solid phase also has a physical interpretation: solid-phase s can be regarded as a measure of the relative strengths of adhesion forces between the liquid and the solid, vs. cohension forces between molecules within the liquid.

The driving force in terms of partial pressures, $\| p - p^* \| \le p_\epsilon$, was used as a convergence criterion of the algorithm. Again, there is a relationship between the numerical criterion p_ϵ and a real physical quantity—the potential barrier to phase transition, which reveals itself by the existence of oversaturated vapors and metastable liquids. The computational algorithm is reproduced in Figure 2. From the computational

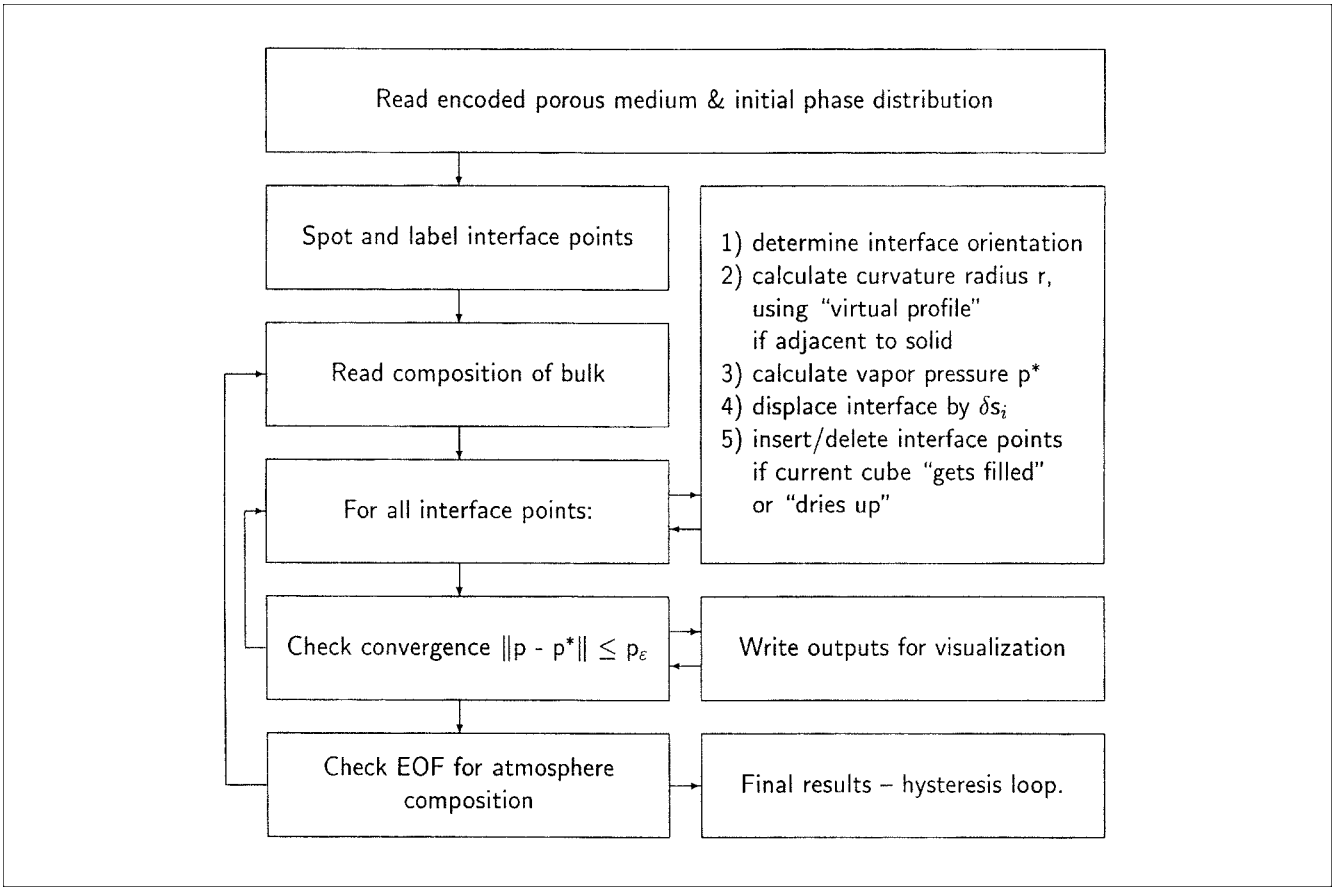

Figure 2. Flow chart of the computational algorithm.

geometry point of view, the algorithm just described represents a variation on the level set approach of Sethian (1996), whereby an interface evolves with a curvature-dependent velocity so as to reach an equilibrium shape, which represents the local minimum of a "global" function, the Gibbs energy in this case. From the point of view of nonequilibrium thermodynamics, the linear relationship (Eq. 5) can be thought of as a first-order term in the expansion of the Gibbs energy along its minimum, with respect to interface position.

Results and Discussion

Water was chosen as the adsorbate because the system water–silica gel is well known to reveal hysteresis (Rajniak and Yang, 1994), and knowledge of the shape and temperature dependence of adsorption equilibrium isotherms of water on silica gel is crucial for a proper description of the pressure swing adsorption process for air drying (Štěpánek et al., 1999). The properties of various adsorbent materials were simulated by assuming a general Gaussian-correlated random medium (Adler and Thovert, 1998) with different porosity and pore-space correlation length, and varying the wetting angle.

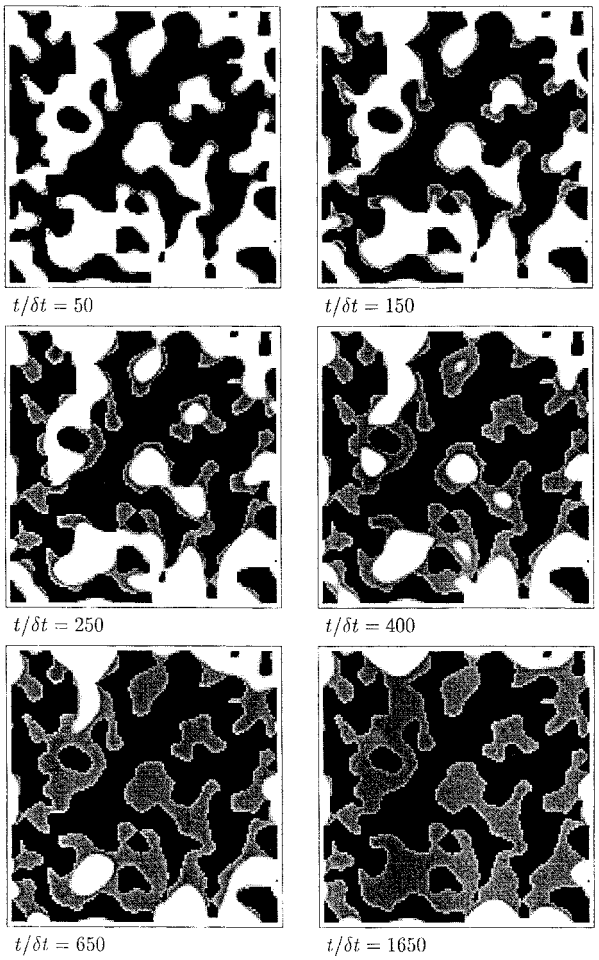

Figure 3. Convergence of the computational algorithm toward equilibrium distribution of condensate, starting from an initially " dry" medium.

Data are for water at 25°C: $P = 10^5$ Pa, $\varphi = 80\%$, $\vartheta = \pi/10$; $L_c = 8$ nm, $\epsilon = 0.55$. The porous medium is 3-D with translational symmetry in the z-direction. Black means solid, grey liquid, and white vapor.

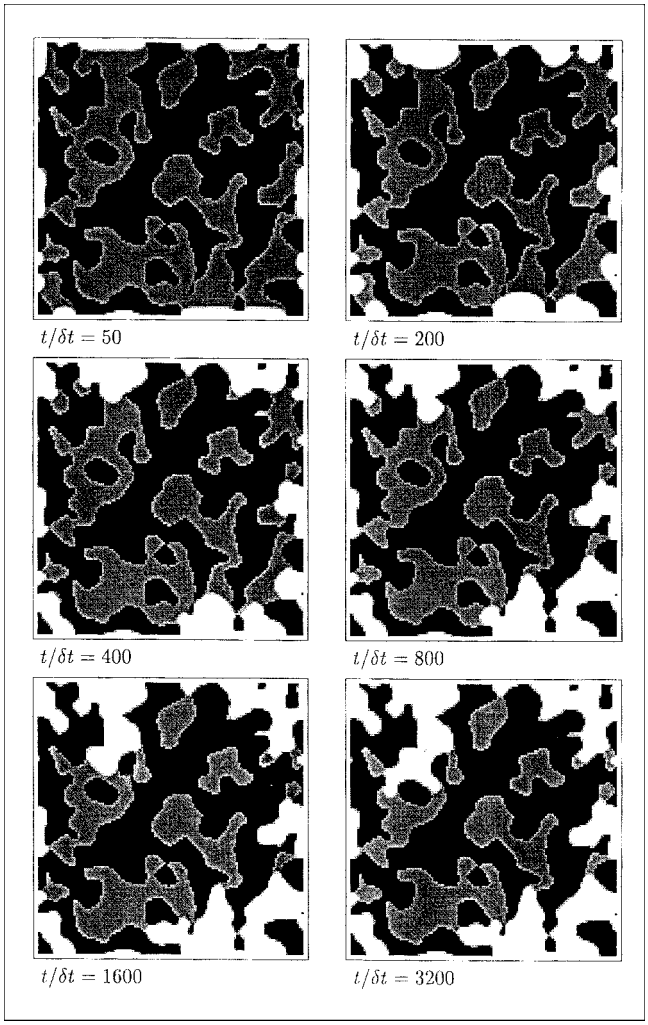

Figure 4. Time steps of the numerical sequence during the calculation of equilibrium condensate distribution, starting from an initially fully loaded sample.

Conditions are the same as in Figure 3, only $\varphi = 20\%$. Notice the relatively high residual loading, due to many "bottle shaped" pores with narrow openings.

Figures 3 and 4 illustrate the progress of the computational algorithm during two typical situations: the filling of pores by condensate when starting from an initially empty porous medium surrounded by atmosphere with high relative humidity, and pore emptying (evaporation of condensate) when starting from an initially fully loaded porous sample immersed in a low-humidity atmosphere. The porous medium shown in Figures 3 and 4 is a Gaussian-correlated 2-D medium (pore-space correlation length $L_c = 8$ nm, porosity $\epsilon = 0.55$) extruded to the third dimension along the z-axis; therefore, all sections parallel to the x-y plane are identical and no closed cavities emerge during condensation because

the bulk gas phase is always accessible in the z-direction. In agreement with Eqs. 3 and 5, the smallest pores (where the driving force for condensation is the highest) get filled first, followed by larger pores. Notice (such as on panel $t/\partial t = 400$ of Figure 3) that when originally independent liquid–vapor interfaces merge into a single interface, they tend to form a geometrically regular shape (cylinder in the case of extruded 2-D medium) relatively fast. This is a consequence of the curvature-dependent velocity of interface growth, a key property of the employed numerical algorithm. The initially independent interfaces have generally different shapes and orientations, determined by the geometry of the pores from which they have emerged. As they join, sharp-curvature manifolds can form as a result of different interface orientations. The small curvature radius in these parts of the newly created interface implies a higher driving force term in Eq. 5, hence faster interface growth, which continues until the interface curvature (thus the speed of growth) is approximately the same in all points along the interface.

Wetting of the solid by the liquid (as quantified by the contact angle) demonstrates itself well in the evaporation iteration sequence, displayed in Figure 4. The interface is initially flat (initial conditions: pore space completely filled by condensate), thus the rate of evaporation is the same all along the interface. For liquids wetting the solid (that is, having small contact angle, which is also the case shown in Figure 4), the liquid–vapor interface adjacent to the solid phase becomes more curved (cf. Eq. 6), the rate of evaporation decreases locally, and a characteristic meniscus forms. Depending on the orientation of the solid–fluid interface vs. the liquid–vapor interface, the evaporation either continues or the meniscus reaches an equilibrium shape, that is, such that the liquid–vapor interface spans from solid to solid, satisfying the wetting angle at all contact lines and having a mean curvature radius in equilibrium with the partial pressure of the vapor, according to Eq. 3. The requirement on the mean interface curvature radius provides many degrees of freedom for the interface arrangement, so that an equilibrium shape can be attained in almost any geometry for a wide range of wetting angles (cf. also the discussion preceding Eq. 4). Patterns typical for invasion percolation frequently emerge during the evaporation iteration sequence (cf. Guyer and McCall, 1996).

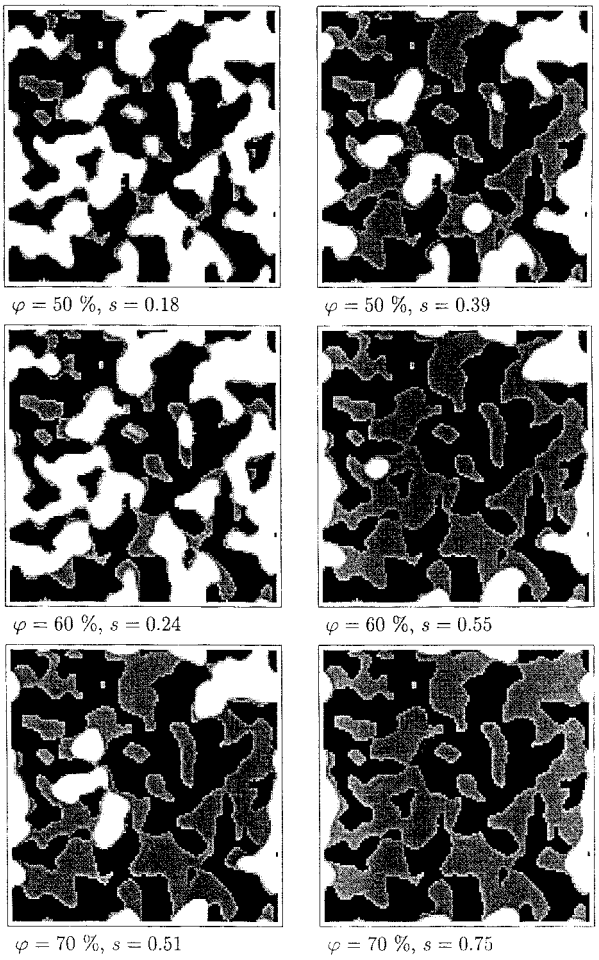

Figure 5. Illustration of hysteresis; phase distributions in equilibrium with φ = 50, 60, and 70%, starting from an initially empty (left column) and fully loaded (right column) medium.

The figures represent sections through a truly 3-D medium ($L_c = 12$ nm, $\epsilon = 0.50$), therefore interface curvatures can have seemingly "nonequilibrium" shapes.

Hysteresis

All subsequent simulations were performed in samples of 3-D reconstructed porous media, that is, with geometry varying in all three orthogonal directions. The large number of possible equilibrium arrangements of condensate in such media creates conditions for the existence of hysteresis. Given the variety of the solid-phase geometry, chances are high that an interface growing from an initially empty medium reaches an equilibrium configuration that is different from that which is arrived at from an initially fully loaded sample. This is demonstrated in Figure 5, which shows the distribution of condensate in a sample of porous medium (Gaussian-correlated 3-D), in equilibrium with air at different relative humidities (50, 60, and 70%), starting from an initially empty (left column) and fully loaded (right column) pore space. The condensate distributions shown in Figure 5 are limiting cases, they correspond to points on the so-called primary adsorption and primary desorption isotherms (the envelope of the main hysteresis loop). Taking, for example, the case of primary desorption, the configurations shown in Figure 5 are the first to which the algorithm has converged (that is, they satisfy the equilibrium conditions) during evaporation. But as may be suspected from the relatively large difference between each of the two images corresponding to the same relative humidity in Figure 5 ($\Delta s = 0.21$, 0.31, and 0.24 for $\varphi =$ 50, 60, and 70%, respectively), more equilibrium distributions can exist between the two limiting cases (theoretically a continuum). The rich geometry of the solid/fluid phase boundary provides for such equilibrium condensate distributions (that is, satisfying contact angles and surface curvature).

However, of interest are only those distributions which are physically accessible (that is, they can be obtained by re-

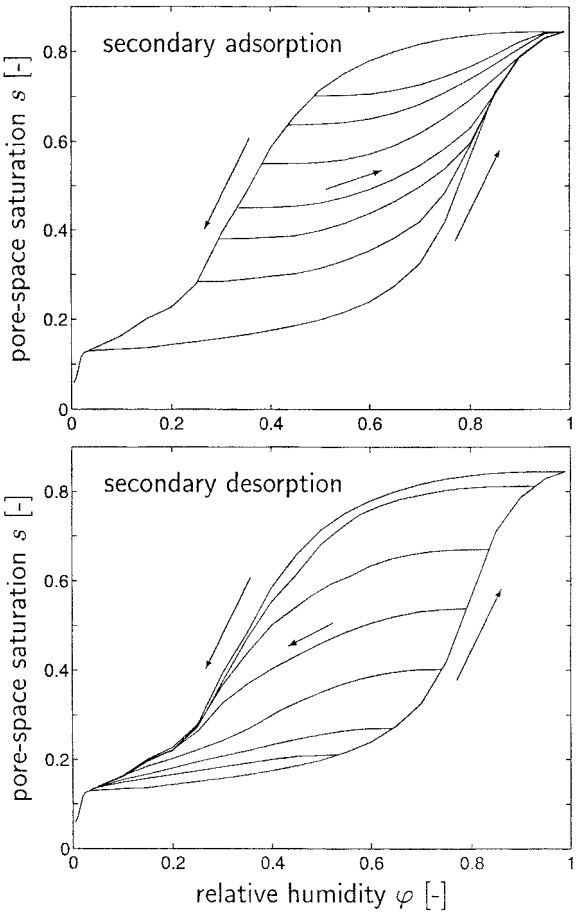

Figure 6. Calculated primary and secondary hysteresis isotherms for a 3-D sample with $\epsilon = 0.50$, L_c = 12 nm, and $\vartheta = \pi/10$ at 25°C.

peated adsorption/desorption cycles with different relative humidities, starting either from an initially empty or fully loaded adsorbent particle). The plots of the fraction of pore space filled at equilibrium vs. relative humidity of the surrounding air for these allowable phase distributions are llustrated in Figure 6 for a porous sample with the same statistical properties (porosity, pore-space correlation length) as that from Figure 5, but relatively large in size ($120 \times 120 \times 120$ unit cubes) in order to obtain smooth curves and eliminate the effects of filling and emptying of individual pores. The curves starting on the primary adsorption isotherm, but lower than the upper closure point of the main hysteresis loop, are called secondary desorption curves; analogously for curves originating on the primary desorption branch. Tertiary and higher-order isotherms can be constructed analogously. Figure 6 reveals that, for this particular medium-adsorbate couple, the hysteresis loop (type IV according to IUPAC classification) is relatively wide both in terms of the span of relative humidities and the difference between the amount adsorbed for points inside the hysteresis loop. The influence of geometrical properties of the porous medium on the shape of the hysteresis loop is discussed in detail below.

Effects of physicochemical properties

Let us now investigate the effect of two physicochemical parameters—the wetting angle and temperature—on the hysteresis behavior. The influence of the liquid–solid contact angle ($\vartheta < 90°$ for hydrophilic materials, $\vartheta > 90°$ for hydrophobic ones) is plotted in Figure 7. The graph shows points on the primary desorption branch for different wetting angles and relative humidities of the vapor phase. For all relative humidities, the fraction of pore space filled, s, decreases with increasing wetting angle ϑ. This trend can be well explained by tracking an individual evaporating interface, descending through an isolated pore. While in a highly wettable solid (small ϑ), the liquid tends to "stick" to the solid, which leads to a small curvature radius relatively soon, and the interface does not have to penetrate too deep into the pore in order to find its equilibrium shape; larger contact angles cause the liquid to be "pushed away" by the solid, which keeps the interface relatively flat (and the driving force for evaporation correspondingly high) for a long time during its penetration through the pore. It may happen for larger contact angles that an equilibrium interface shape is not reached at all and the whole pore is emptied. As can be seen in Figure 7, this is the case, for example, for $\varphi = 20\%$ and $\vartheta > 60°$, where only a small ($\sim s < 0.02$) residual loading remains in the pore space, corresponding only to the narrowest dead ends of pores. It is interesting to observe that the effect of the contact angle is rather uneven for the various relative humidities considered in this example. Whereas for the case $\varphi = 80\%$, the decrease of the loading s between $\vartheta = 10°$ and $\vartheta = 80°$ is relatively small (from $s = 0.88$ to $s = 0.66$, being 25%), the wetting angle has a much more significant impact around the widest part of the hysteresis loop, for $\varphi = 50\%$ (cf. Figure 6), where the difference in residual loading is as high as 92% ($s = 0.65$ for $\vartheta = 10°$ and $s = 0.05$ for $\vartheta = 80°$).

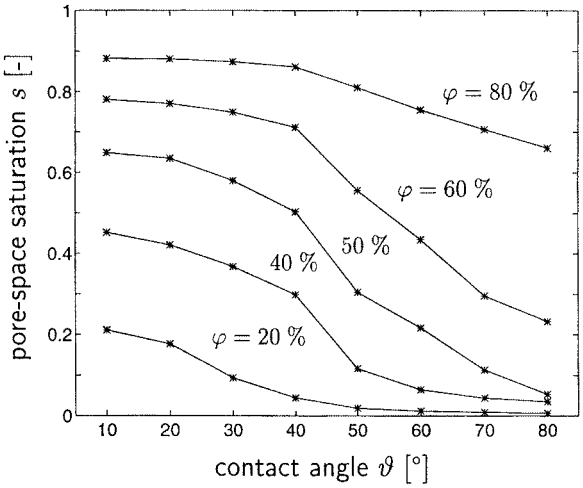

Figure 7. The influence of the wetting angle ϑ on the fraction of pore-space-filled s in equilibrium with relative air humidities φ = 20, 40, 50, 60 and 80%, starting from an initially fully loaded medium (that is, points on the primary desorption isotherm). Porous sample properties are the same as in Figure 6.

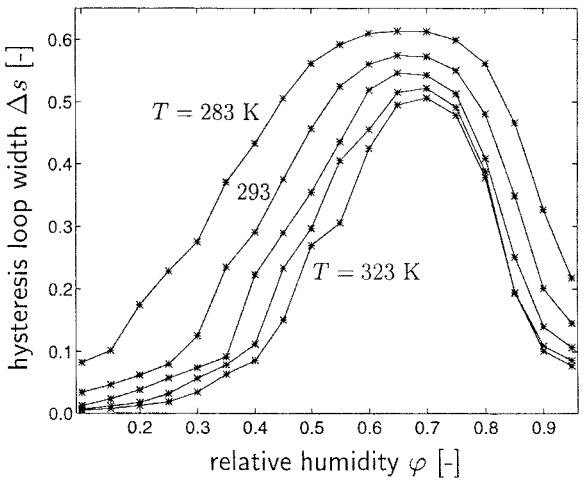

Figure 8. Temperature dependence of the width of the main hysteresis loop.

$\Delta s \equiv s_D - s_A$, where s_A and s_D are points on the primary adsorption and desorption isotherms, respectively. Porous sample properties are the same as in Figure 6.

The effect of temperature on the width of the main hysteresis loop is summarized in Figure 8 (Δs is the difference between the primary desorption and primary adsorption isotherms). The trend is rather obvious—the hysteresis effect tends to be smaller for higher temperatures, as could be expected from the fact that at higher temperatures the equilibrium vapor pressure p^* increases (both due to higher p_s and an increase in the exponential term of Eq. 3), thus effectively reducing the fraction of pore space in which condensation can occur for any given gas-phase composition. Both the width and ''amplitude'' of the Δs graphs monotonously decrease with increasing temperature. However, the rate of decrease is not the same in all parts of the hysteresis loop. While in the region of higher relative humidities ($\varphi = 70-90\%$), the decrease of Δs is only significant at lower temperatures ($T =$ 283–293 K), it virtually stops for higher temperatures. On the other hand, for relative humidities in the lower range ($\varphi =$ 30–45%), the effect of temperature increase is very strong, and it almost eliminates hysteresis ($\Delta s < 0.15$) for higher temperatures.

Effects of geometry

Apart from a general Gaussian-correlated random 3-D medium, several regular (random and deterministic, both classic and fractal) media were tested in order to investigate the influence of the geometry of the medium on the shape of hysteresis isotherms. The significance of such a study is twofold; first, measuring adsorption/desorption hysteresis is nowadays a standard procedure for the characterization of microporous materials (pore-size distribution is evaluated from the BET isotherms). The identification of links between the morphology of a porous medium and the types of hysteresis isotherms is thus of importance for the interpretation of experimental data. Second, sol-gel and other techniques are becoming available for the preparation of controlled porous structures at the submicron length scales (Biz and Ocelli, 1998; Yang et al., 1998). Porous media with predetermined geometric properties (thus predetermined hysteresis behavior) could then serve, for example, for temperature-controlled release of active components or for air-conditioning applications in special atmospheres.

Let us first consider the case of a porous medium reconstructed from a Gaussian-correlated random field. Two parameters characterizing the medium were varied; the porosity ϵ (zeroth moment of the phase function) and the so-called correlation length L_c (first central moment of X)—for exact definitions, see Adler and Thovert (1998). Figures 9a and 9b summarize the influence of these two parameters on the hysteresis behavior. The correlation length determines the partial pressure by which condensation occurs in most of the pore space, according to Eq. 3. This can be clearly seen in Figure 9b, where the capillary upswing moves toward higher relative humidities with increasing L_c. The adsorption branch gradually changes from type-IV to type-II isotherm as L_c increases from 9 to 12 to 18 nm, because in large pores condensation does not occur in a significant extent until relative humidity approaches $\varphi \to 1$. This trend is valid for both the sample with porosity $\epsilon = 0.35$ and a high-porosity one with $\epsilon = 0.65$. The main difference between the two cases is in the vertical position of the adsorption branches (their relative adsorption capacity); for the same correlation length, say $L_c = 9$ nm, the pore space of the sample with porosity $\epsilon = 0.35$ has a higher relative amount adsorbed s for any given vapor relative saturation than that with $\epsilon = 0.65$. This fact can be explained as follows. In a high-porosity sample, many independent pores with dead ends form the pore space, while in a low-porosity sample having the same correlation length, the pore space is more compact and individual ''pores'' can no longer be distinguished. Therefore, when condensation occurs in a region of partial pressures corresponding to the correlation length, a significant part of the low-porosity sample is filled by condensate (the originally distinct interfaces growing from smaller convex dead ends join to form a single interface, which continues to minimize the surface/volume ratio). In the highly porous sample, on the other hand, the condensate remains disconnected even if a majority of pores fill up, because the individual pores are ''scattered around.'' The desorption branches (Figure 9a) also show the effect of increasing the correlation length on shifting the capillary desorption downswing toward higher partial pressures. Apart from this general trend, an interesting phenomenon is the qualitative change in the type of hysteresis loop; while the case $\epsilon = 0.35$, $L_c = 9$ nm clearly shows an H2 hysteresis loop (according to IUPAC classification), an increase in the porosity and the correlation length causes the primary desorption branch to change from concave ($\partial^2 s/\partial\varphi^2 < 0$) to convex ($\partial^2 s/\partial\varphi^2 > 0$) at $\varphi \to 1$, hence the H3 hysteresis loop for $\epsilon =$ 0.65 and $L_c = 18$ nm.

A general Gaussian-correlated random medium contains approximately the same proportion of concave and convex solid–fluid interfaces. This is not the case for all porous media, though; depending on the processes that lead to the formation of the porous medium (repeated sol-gel transition, precipitation, leaching during activation, etc.), its geometry can also contain either predominantly concave (such as the pore space between packed spheres, cf. Pilotti, 1998) or convex (such as in a solid foam, such as Park and Xia, 1998)

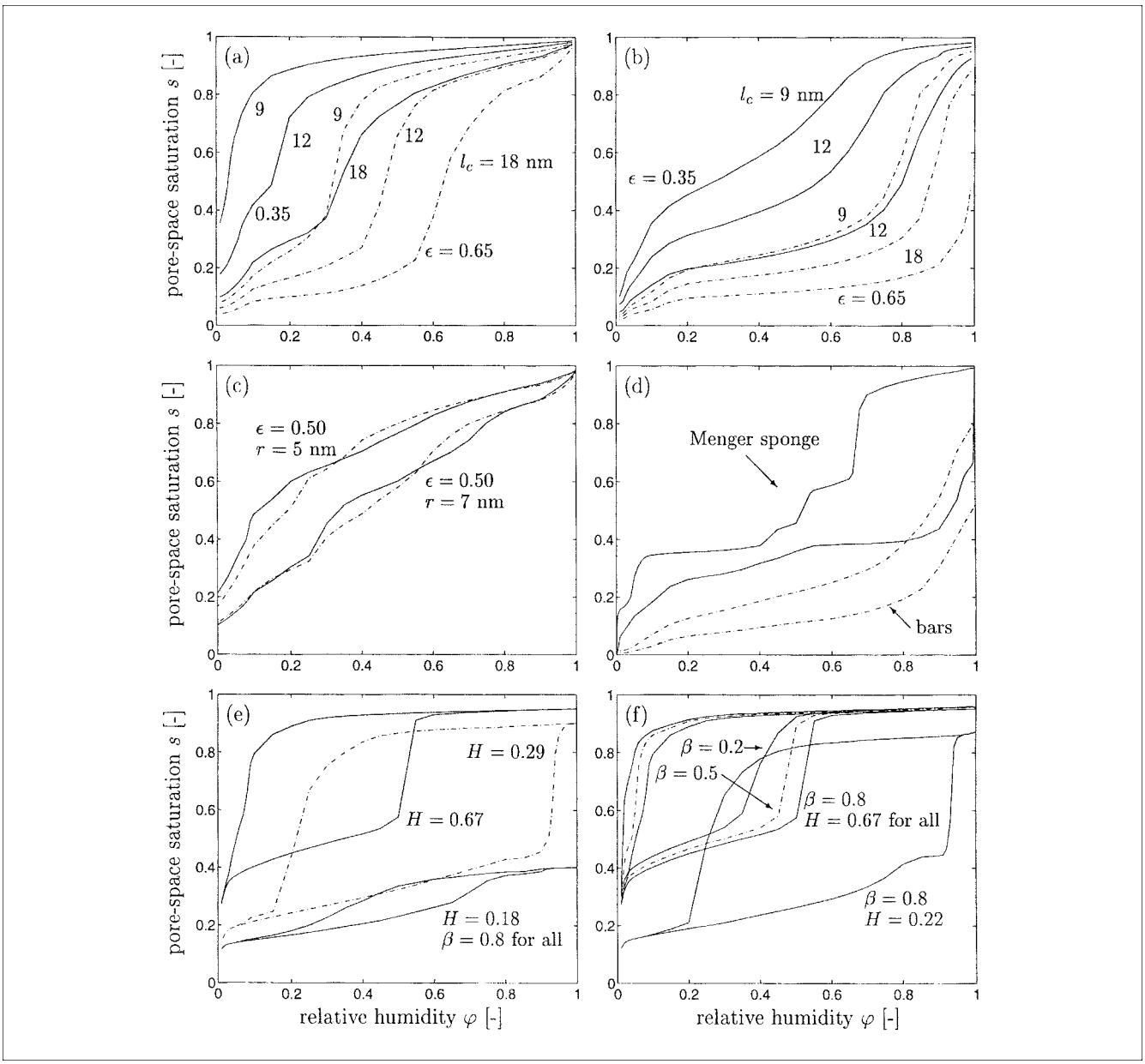

Figure 9. Summary of hysteresis curves for various geometries.

(a) Primary desorption, and (b) primary adsorption isotherms for a Gaussian-correlated random medium; (c) primary desorption curves for randomly displaced spheres; (d) main hysteresis loop for a Menger sponge and primary adsorption curves for randomly oriented bars; (e) and (f) main hysteresis loops for an aperture between two self-affine fractal surfaces.

interfaces. A porous medium created by randomly displaced spheres (either with constant radius or satisfying certain distribution of radii) was considered as a model system for these two cases. The spheres were allowed to overlap. Solid spheres represent a system with concave interfaces, void spheres within a surrounding solid represent a convex system. A cross section through such a model porous medium is shown in Figure 10a. The effect of convexity vs. concavity of the porous space is shown in Figure 9c, where the primary desorption isotherms are plotted; solid lines correspond to solid spheres, dashed lines to void spheres. Porosity was $\epsilon = 0.50$ in all cases, sphere radii $r = 5$ and 7 nm. Three characteristic regions can be distinguished along the desorption isotherms, following from $\varphi = 1$ toward $\varphi = 0$. For higher relative humidities, both isotherms are identical (that is, the geometry has no effect); in this region the liquid–vapor interface delimiting the initially fully loaded porous sample only increases its curvature, but pore emptying does not yet occur. As the relative humidity further decreases, the V-shaped interspherical pores start to empty first (cf. the preceding discussion of the effects of the contact angle), while in the case of void spheres, the meniscus only continues to increase its curvature without descending into the cavities. Therefore, the relative loading is higher in this region for convex pore geometry than for the concave one. For even lower values of φ, the situation reverses and higher residual loading remains in the narrow ends

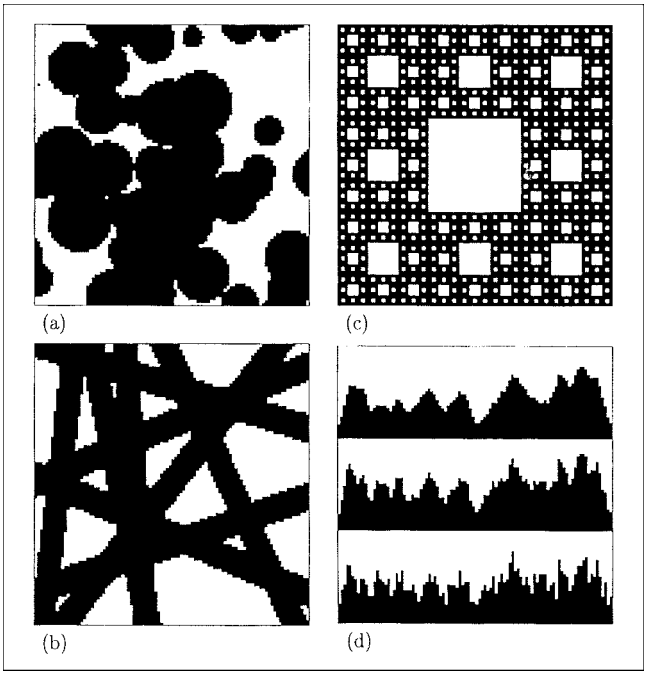

Figure 10. Examples of model porous media.

(a) Randomly displaced spheres; (b) simulated nanofibrilous material; (c) the Menger sponge; (d) self-affine random fractal surface (Hurst exponents $H = 0.18$, 0.29, and 0.67, from top to bottom).

between neighboring spheres, while the round ''pores'' represented by spherical cavities are emptied.

The next model geometry was a porous medium created by randomly oriented rectangular bars, positioned parallel to the *x-y* plane (Figure 10b). Such system is an approximation of fibrilous materials (Termonia, 1997), used, for example, for microfiltration membranes. The variable parameters were the overall porosity, and the dimensions of the bars (height and width). Contrary to what one might expect from the shape of the basic building block (a rectangular bar), the hysteresis behavior of this porous medium was not found to be substantially different from that of a general Gaussian random medium (at least up to certain limiting porosity—representing a percolation threshold for the solid phase—above which the connected system of bars breaks down into a discontinuum of individual bars, providing no support for the onset of capillary condensation). The reason for the qualitatively similar behavior is that the random orientation of the bars provides a wide range of V-shaped pores of different angles in which capillary condensation can occur. The condensate effectively ''rounds off'' the initially rectangular medium. The two dashed curves shown in Figure 9d are primary adsorption isotherms corresponding to porosity $\epsilon = 0.50$ and bar dimensions 9×5 and 15×7 nm. The upper curve corresponds to the smaller bars; to achieve the same porosity, more of the smaller bars have to be placed in a unit volume of medium, thus providing more ''sites'' for capillary condensation (cf. the earlier discussion of the influence of porosity and the pore-space correlation length on hysteresis in a Gaussian medium.)

Figure 9d also shows a hysteresis curve (solid line) for a deterministic fractal—the Menger sponge (cross section shown in Figure 10c). The Menger sponge is formed by removing later generations of smaller cubes (one-third the size of the parent generation) from the center of the cube. The pore-size distribution is thus rather specific; each generation contains square pores of sides equal to one-third of those of the parent generation, their total pore volume being 20/27 of that of the parent generation. During condensation, liquid interfaces first start growing in the corners of the square channels (this phase corresponds to a slight plateau on the primary adsorption curve, the length of this plateau being proportional to the size of the pore), forming a cylindrical meniscus as interfaces growing from opposite sides merge, and eventually filling the whole pore. The primary adsorption curve is thus relatively smooth. During evaporation from a Menger sponge initially filled by condensate, the effect of the stepwise PSD is more pronounced, demonstrating itself in the form of long plateaus followed by steep drops in the amount adsorbed. Smaller, secondary steps can also be observed that are caused by the fact that the walls of the square pores contain ''windows'' into next-generation pores, filled by liquid. The interaction of the vapor–liquid interface with these pore openings causes the secondary steps on the desorption branch. The curve shown in Figure 9d was calculated for a five-generation fractal; due to the large differences in the pore sizes of subsequent generations, though, only the emptying of three generations of pores (plus one secondary step, as discussed earlier) is visible; the smallest pores empty only as $\varphi \to 0$.

Finally, a geometry represented by a fracture limited by two self-affine random fractal surfaces was considered. The surfaces of pores within porous materials are often fractal (that is, they have a noninteger dimension between 2 and 3), and adsorption measurements provide a means of estimating their fractal dimension (such as Lee (1998) and references therein). Examples of three such surfaces with various roughnesses, viewed from the side, are shown in Figure 10d. The roughness of the surface is characterized by the so-called Hurst exponent, H (see Mourzenko et al. (1999) for exact definitions). In addition, the top and bottom surfaces of a fracture can be correlated by a coefficient $\beta \in \langle 0; 1 \rangle$. Typical results of the studies that were performed are summarized in Figures 9e and 9f. The fracture amplitude (the difference between the highest point of the upper surface and the lowest points of the lower surface) was 8 nm in all cases; the Hurst exponent and surface correlation were systematically varied. The hysteresis loops from Figure 9e show the effect of decreasing surface fractality for a well-correlated fracture ($\beta = 0.8$). Two qualitatively different regions can be distinguished on the primary adsorption isotherm. At lower partial pressures, capillary condensation occurs independently in the fractal pore space of the lower and upper surfaces. Above a certain critical value of φ, condensate from the upper and lower surfaces grow together at places where the fracture aperture is small, causing a sudden ''flooding'' by condensate of the whole fracture (with the exception of some enclosed cavities). This capillary upswing is so sharp because the relative humidity at which the initiating event happens (that is, liquid interface growing from one surface reaches a solid point of the opposite surface) is above the value that would corre-

spond to a curvature radius covering the fracture opening. The φ value corresponding to this radius is in fact rather low, as can be seen from the onset of the capillary downswing on the primary desorption branch. As the surface becomes less rough, there are fewer possibilities for a growing interface to reach an extremity of the opposite solid wall, and the critical relative humidity shifts toward higher values (cf. cases $H = 0.67$ and $H = 0.29$ from Figure 9e). For very smooth surfaces (provided that they are sufficiently correlated, which is the case when $\beta = 0.8$, as in Figure 9e), it can happen that condensates from opposite surfaces never form a single phase, in which case only a narrow hysteresis loop remains and fracture filling does not occur. An intermediate case ($H = 0.22$, $\beta = 0.8$) is shown in Figure 9f, where there is an obvious plateau on the primary adsorption branch just before the capillary upswing, corresponding to the almost saturated capacity of the fractal surface. There are in fact two superimposed hystereses, one resulting from the local fractal geometry of the surfaces, the other being caused by the filling of the bulk fracture pore space. Such multiple-hysteresis phenomena are characteristic of multiple-scale porous media. Figure 9f also shows the influence of the correlation between the surfaces for a constant value of the Hurst exponent ($H = 0.67$ for the bundle of three hysteresis loops from the figure). Fractures with low β provide a larger number of possible ''penetration points,'' that is, such places where a peak from one surface reaches into a region in the pore space of the other surface, which fills by capillary condensation relatively early. Such a place then serves as a support for fracture-wide condensation. A larger number of such nucleation centers also cause the upswing part on the primary adsorption branch to be less steep (case $\beta = 0.2$ in Figure 9f).

Conclusions

Only the contribution of capillary condensation to the total amount of adsorbate present in the porous space of an adsorbent particle is treated in this work. However, in the region of low partial pressures, where the volume of condensate (and so the fraction of pore space filled) is small, the contribution of ''real'' surface adsorption to the total amount adsorbed is proportionally more significant. Since the model adopted here is inherently continuous, the lower length-scale limits of its applicability also have to be kept in mind. Phenomena in pores with characteristic dimensions of less than about 30 molecular diameters should preferentially be modeled by MC/MD approaches, because macroscopic quantities such as surface tension and wetting angle lose their meaning at these length scales. Being aware of the validity limits imposed upon the model by the underlying physical assumptions (continuum), the model represents a versatile tool for the prediction of hysteresis behavior in adsorption systems dominated by capillary condensation in meso-/micropores.

The main advantage of the algorithm presented in this work is that it provides a relatively very rapid means of estimating adsorption isotherms in the presence of capillary condensation (compared with rigorous, but computationally rather demanding Monte Carlo simulations, which are limited to the smallest length scales and generally can provide no information about the dynamics), its inputs being only readily available physicochemical properties of the condensate and knowledge about the pore-space geometry. It can thus be easily integrated into a multiple-scale computational framework for the modeling of industrial processes employing porous materials, be it adsorption-based separation or heterogeneous catalysis.

Acknowledgments

Financial support from Project VS 96073 (Czech Ministry of Education), Grant 104/99/1408 (Czech Grant Agency), and Bourse du Gouvernement Français 11874, is gratefully acknowledged.

Notation

G = Gibbs energy, J
h = size of volume element, m
k = kinetic constant, mol/m·s
p = partial pressure, Pa
R = molar gas constant, J/K·mol
s = total fraction of pore-space filled (saturation)
t = iteration time, s
z = spatial coordinate, m

Literature Cited

Adler, P. M., ''The Method of Reconstructed Porous Media,'' *Curr. Top. Phys. Fluids*, **1**, 277 (1994).
Adler, P. M., and J.-F. Thovert, ''Real Porous Media: Local Geometry and Macroscopic Properties,'' *Appl. Mech. Rev.*, **51**, 537 (1998).
Ball, P. C., and R. Evans, ''Temperature Dependence of Gas Adsorption on a Mesoporous Solid: Capillary Criticality and Hysteresis,'' *Langmuir*, **5**, 714 (1989).
Békri, S., J.-F. Thovert, and P. M. Adler, ''Dissolution of Porous Media,'' *Chem. Eng. Sci.*, **50**, 2765 (1995).
Biz, S., and M. L. Ocelli, ''Synthesis and Characterization of Mesostructured Materials,'' *Catal. Rev. Sci. Eng.*, **40**, 329 (1998).
Bordère, S., P. L. Llewellyn, F. Rouquerol, and J. Rouquerol, ''Multiple Features of a Porous Structure as Assessed from the Hysteresis of Nitrogen Adsorption-Desportion: Case Study of the Formation of UO_3 from $UO_2(NO_3)_2 \cdot 6H_2O$,'' *Langmuir*, **14**, 4217 (1998).
Deem, M. W., ''Recent Contributions of Statistical Mechanics in Chemical Engineering,'' *AIChE J.*, **44**, 2569 (1998).
Dobbs, H. T., G. A. Darbellay, and J. M. Yeomans, ''Capillary Condensation Between Spheres,'' *Europhys. Lett.*, **18**, 439 (1992).
Fredd, Ch. N., and H. S. Fogler, ''Influence of Transport and Reaction on Wormhole Formation in Porous Media,'' *AIChE J.*, **44**, 1933 (1998).
Gelb, L. D., and K. E. Gubbins, ''Characterization of Porous Glasses: Simulation Models, Adsorption Isotherms, and the Brunauer-Emmett-Teller Analysis Method,'' *Langmuir*, **14**, 2097 (1998).
Guyer, R. A., and K. R. McCall, ''Capillary Condensation, Invasion Percolation, Hysteresis, and Discrete Memory,'' *Phys. Rev. B: Condens. Matter*, **54**, 18 (1996).
Jaroniec, M., ''Fifty Years of the Theory of the Volume Filling of Micropores,'' *Adsorption*, **3**, 187 (1997).
Kainourgiakis, M. E., E. S. Kikkinides, A. K. Stubos, and N. K. Kanellopoulos, ''Adsorption-Desorption Gas Relative Permeability Through Mesoporous Media—Network Modelling and Percolation Theory,'' *Chem. Eng. Sci.*, **53**, 2353 (1998).
Keil, F. J., ''Modelling of Phenomena within Catalyst Particles,'' *Chem. Eng. Sci.*, **51**, 1543 (1996).
Lee, Ch.-K., ''Fractal Surface Analysis by Using Capillary Condensation Data,'' *Ind. Eng. Chem. Res.*, **37**, 3939 (1998).
Liu, H., L. Zhang, and N. A. Seaton, ''Characterization of Mesoporous Solids Using Sorption Hysteresis Measurements,'' *Stud. Surf. Sci. Catal.*, **87**, 129 (1994).
López-Ramón, M. V., J. Jagiello, T. J. Bandosz, and N. A. Seaton, ''Determination of the Pore Size Distribution and Network Connectivity in Microporous Solids by Adsorption Measurements and Monte Carlo Simulation,'' *Langmuir*, **13**, 4435 (1997).
Mourzenko, V. V., Thovert, J.-F., and Adler, P. M., ''Percolation

and Conductivity of Self-Affine Fractures,'' *Phys. Rev. E*, **59**, 4265 (1999).
Mann, R., ''Computer-Aided Characterization and Design of Catalyst Pore Structure,'' *Structured Catalysts and Reactors*, A. Cybulski and J. A. Moulijn, eds., Dekker, New York (1998).
Müller, E. A., L. F. Rull, L. F. Vega, and K. E. Gubbins, ''Adsorption of Water on Activated Carbons: A Molecular Simulation Study,'' *J. Phys. Chem*., **100**, 1189 (1996).
Okazaki, M., ''Roles of Capillary Condensation in Adsorption,'' *Stud. Surf. Sci. Catal.*, **80**, 13 (1993).
Ostrovskii, N. M., N. M. Bukhavtsova, and V. K. Duplyakin, ''Catalytic Reactions Accompanied by Capillary Condensation. 1. Formulation of the Problems,'' *React. Kinet. Catal. Lett.*, **53**, 253 (1994).
Park, S. H., and Y. Xia, ''Fabrication of Three-Dimensional Macroporous Membranes with Assemblies of Microspheres as Templates,'' *Chem. Mater.*, **10**, 1745 (1998).
Pilotti, M., ''Generation of Realistic Porous Media by Grains Sedimentation,'' *Transport Porous Media*, **33**, 257 (1998).
Rajniak, P., and R. T. Yang, ''Hysteresis-Dependent Adsorption-Desorption Cycles: Generalization for Isothermal Conditions,'' *AIChE J.*, **40**, 913 (1994).
Ravikovitch, P. I., G. L. Haller, and A. V. Neimark, ''Adsorption Characterization of Mesoporous Molecular Sieves,'' *Stud. Surf. Sci. Catal.*, **117**, 77 (1998).
Seri-Levy, A., and D. Avnir, ''Surface Geometry Effects on Adsorption-Desorption Hysteresis, Latent Adsorption and Adsorption-Probability Plots,'' *Stud. Surf. Sci. Catal.*, **80**, 365 (1993).
Sethian, J. A., *Level Set Methods: Evolving Interfaces in Geometry, Fluid Mechanics, Computer Vision, and Material Science*, Cambridge Univ. Press, Cambridge (1996).
Silverstein, D. L., and T. Fort, ''A Numerical Model for Predicting Air-Water Interfacial Area and Water Configuration in Water Wetted Unsaturated Porous Media,'' *AIChE Meeting*, Miami Beach, FL (1998).
Sonwane, C. G., and S. K. Bhatia, ''Adsorption in Mesopores: A Molecular-Continuum Model with Application to MCM-14,'' *Chem. Eng. Sci.*, **53**, 3143 (1998).
Štěpánek, F., M. Kubíček, M. Marek, P. Rajniak, M. Šoóš, and R. T. Yang, ''On the Modeling of PSA Cycles with Hysteresis-Dependent Isotherms,'' *Chem. Eng. Sci.*, (1999).
Termonia, Y., ''Permeability of Sheets of Nonwoven Fibrous Media,'' *Chem. Eng. Sci.*, **52**, 1163 (1997).
Vlachos, D. G., ''Multiscale Integration Hybrid Algorithms for Homogeneous-Heterogeneous Reactors,'' *AIChE J.*, **43**, 3031 (1997).
Yang, P., T. Deng, D. Zhao, P. Feng, D. Pine, B. F. Chmelka, G. M. Whitesides, and G. D. Stucky, ''Hierarchically Ordered Oxides,'' *Science*, **282**, 2244 (1998).
Zhou, W., H. H. A. Hunter, P. A. Wright, Q. Ge, and J. M. Thomas, ''Imaging the Pore Structure and Polytypic Integrowths in Mesoporous Silica,'' *J. Phys. Chem. B*, **102**, 6933 (1998).

Manuscript received Feb. 16, 1999, revision received May 27, 1999.